

# Measurement of $\mathcal{B}(D_s^+ \rightarrow \ell^+ \nu)$ and the Decay Constant $f_{D_s^+}$ From 600 pb<sup>-1</sup> of $e^+e^-$ Annihilation Data Near 4170 MeV

J. P. Alexander,<sup>1</sup> D. G. Cassel,<sup>1</sup> J. E. Duboscq,<sup>1,\*</sup> R. Ehrlich,<sup>1</sup> L. Fields,<sup>1</sup> R. S. Galik,<sup>1</sup>  
L. Gibbons,<sup>1</sup> R. Gray,<sup>1</sup> S. W. Gray,<sup>1</sup> D. L. Hartill,<sup>1</sup> B. K. Heltsley,<sup>1</sup> D. Hertz,<sup>1</sup>  
J. M. Hunt,<sup>1</sup> J. Kandaswamy,<sup>1</sup> D. L. Kreinick,<sup>1</sup> V. E. Kuznetsov,<sup>1</sup> J. Ledoux,<sup>1</sup>  
H. Mahlke-Krüger,<sup>1</sup> D. Mohapatra,<sup>1</sup> J. R. Patterson,<sup>1</sup> D. Peterson,<sup>1</sup> D. Riley,<sup>1</sup> A. Ryd,<sup>1</sup>  
A. J. Sadoff,<sup>1</sup> X. Shi,<sup>1</sup> S. Stroiney,<sup>1</sup> W. M. Sun,<sup>1</sup> T. Wilksen,<sup>1</sup> J. Yelton,<sup>2</sup> P. Rubin,<sup>3</sup>  
N. Lowrey,<sup>4</sup> S. Mehrabyan,<sup>4</sup> M. Selen,<sup>4</sup> J. Wiss,<sup>4</sup> R. E. Mitchell,<sup>5</sup> M. R. Shepherd,<sup>5</sup>  
D. Besson,<sup>6</sup> T. K. Pedlar,<sup>7</sup> D. Cronin-Hennessy,<sup>8</sup> K. Y. Gao,<sup>8</sup> J. Hietala,<sup>8</sup> Y. Kubota,<sup>8</sup>  
T. Klein,<sup>8</sup> R. Poling,<sup>8</sup> A. W. Scott,<sup>8</sup> P. Zweber,<sup>8</sup> S. Dobbs,<sup>9</sup> Z. Metreveli,<sup>9</sup> K. K. Seth,<sup>9</sup>  
B. J. Y. Tan,<sup>9</sup> A. Tomaradze,<sup>9</sup> J. Libby,<sup>10</sup> L. Martin,<sup>10</sup> A. Powell,<sup>10</sup> G. Wilkinson,<sup>10</sup>  
H. Mendez,<sup>11</sup> J. Y. Ge,<sup>12</sup> D. H. Miller,<sup>12</sup> V. Pavlunin,<sup>12</sup> B. Sanghi,<sup>12</sup> I. P. J. Shipsey,<sup>12</sup>  
B. Xin,<sup>12</sup> G. S. Adams,<sup>13</sup> D. Hu,<sup>13</sup> B. Moziak,<sup>13</sup> J. Napolitano,<sup>13</sup> K. M. Ecklund,<sup>14</sup>  
Q. He,<sup>15</sup> J. Insler,<sup>15</sup> H. Muramatsu,<sup>15</sup> C. S. Park,<sup>15</sup> E. H. Thorndike,<sup>15</sup> F. Yang,<sup>15</sup>  
M. Artuso,<sup>16</sup> S. Blusk,<sup>16</sup> S. Khalil,<sup>16</sup> J. Li,<sup>16</sup> R. Mountain,<sup>16</sup> K. Randrianarivony,<sup>16</sup>  
N. Sultana,<sup>16</sup> T. Skwarnicki,<sup>16</sup> S. Stone,<sup>16</sup> J. C. Wang,<sup>16</sup> L. M. Zhang,<sup>16</sup> G. Bonvicini,<sup>17</sup>  
D. Cinabro,<sup>17</sup> M. Dubrovin,<sup>17</sup> A. Lincoln,<sup>17</sup> M. J. Smith,<sup>17</sup> P. Naik,<sup>18</sup> J. Rademacker,<sup>18</sup>  
D. M. Asner,<sup>19</sup> K. W. Edwards,<sup>19</sup> J. Reed,<sup>19</sup> A. N. Robichaud,<sup>19</sup> G. Tatishvili,<sup>19</sup>  
E. J. White,<sup>19</sup> R. A. Briere,<sup>20</sup> H. Vogel,<sup>20</sup> P. U. E. Onyisi,<sup>21</sup> and J. L. Rosner<sup>21</sup>

(CLEO Collaboration)

<sup>1</sup>*Cornell University, Ithaca, New York 14853, USA*

<sup>2</sup>*University of Florida, Gainesville, Florida 32611, USA*

<sup>3</sup>*George Mason University, Fairfax, Virginia 22030, USA*

<sup>4</sup>*University of Illinois, Urbana-Champaign, Illinois 61801, USA*

<sup>5</sup>*Indiana University, Bloomington, Indiana 47405, USA*

<sup>6</sup>*University of Kansas, Lawrence, Kansas 66045, USA*

<sup>7</sup>*Luther College, Decorah, Iowa 52101, USA*

<sup>8</sup>*University of Minnesota, Minneapolis, Minnesota 55455, USA*

<sup>9</sup>*Northwestern University, Evanston, Illinois 60208, USA*

<sup>10</sup>*University of Oxford, Oxford OX1 3RH, UK*

<sup>11</sup>*University of Puerto Rico, Mayaguez, Puerto Rico 00681*

<sup>12</sup>*Purdue University, West Lafayette, Indiana 47907, USA*

<sup>13</sup>*Rensselaer Polytechnic Institute, Troy, New York 12180, USA*

<sup>14</sup>*Rice University, Houston, TX 77005, USA*

<sup>15</sup>*University of Rochester, Rochester, New York 14627, USA*

<sup>16</sup>*Syracuse University, Syracuse, New York 13244, USA*

<sup>17</sup>*Wayne State University, Detroit, Michigan 48202, USA*

<sup>18</sup>*University of Bristol, Bristol BS8 1TL, UK*

<sup>19</sup>*Carleton University, Ottawa, Ontario, Canada K1S 5B6*

<sup>20</sup>*Carnegie Mellon University, Pittsburgh, Pennsylvania 15213, USA*

<sup>21</sup>*Enrico Fermi Institute, University of Chicago, Chicago, Illinois 60637, USA*

(Dated: January 9, 2009)

## Abstract

We examine  $e^+e^- \rightarrow D_s^- D_s^{*+}$  and  $D_s^{*-} D_s^+$  interactions at 4170 MeV using the CLEO-c detector in order to measure the decay constant  $f_{D_s^+}$  with good precision. Previously our measurements were substantially higher than the most precise lattice based QCD calculation of  $(241 \pm 3)$  MeV. Here we use the  $D_s^+ \rightarrow \ell^+ \nu$  channel, where the  $\ell^+$  designates either a  $\mu^+$  or a  $\tau^+$ , when the  $\tau^+ \rightarrow \pi^+ \bar{\nu}$ . Analyzing both modes independently, we determine  $\mathcal{B}(D_s^+ \rightarrow \mu^+ \nu) = (0.565 \pm 0.045 \pm 0.017)\%$ , and  $\mathcal{B}(D_s^+ \rightarrow \tau^+ \nu) = (6.42 \pm 0.81 \pm 0.18)\%$ . We also analyze them simultaneously to find an effective value of  $\mathcal{B}^{\text{eff}}(D_s^+ \rightarrow \mu^+ \nu) = (0.591 \pm 0.037 \pm 0.018)\%$  and  $f_{D_s^+} = (263.3 \pm 8.2 \pm 3.9)$  MeV. Combining with the CLEO-c value determined independently using  $D_s^+ \rightarrow \tau^+ \nu$ ,  $\tau^+ \rightarrow e^+ \nu \bar{\nu}$  decays, we extract  $f_{D_s^+} = (259.5 \pm 6.6 \pm 3.1)$  MeV. Combining with our previous determination of  $\mathcal{B}(D^+ \rightarrow \mu^+ \nu)$ , we extract the ratio  $f_{D_s^+}/f_{D^+} = 1.26 \pm 0.06 \pm 0.02$ . No evidence is found for a CP asymmetry between  $\Gamma(D_s^+ \rightarrow \mu^+ \nu)$  and  $\Gamma(D_s^- \rightarrow \mu^- \nu)$ ; specifically the fractional difference in rates is measured to be  $(4.8 \pm 6.1)\%$ . Finally, we find  $\mathcal{B}(D_s^+ \rightarrow e^+ \nu) < 1.2 \times 10^{-4}$  at 90% confidence level.

---

\*Deceased

## I. INTRODUCTION

We discuss here an improved measurement of the width of the purely leptonic decay  $D_s^+ \rightarrow \ell^+ \nu$ , when the  $\ell^+$  is either a  $\mu^+$  or a  $\tau^+$ , when the latter decays into a  $\pi^+ \bar{\nu}$  [1]. In a companion article [2] we report an improved measurement of the decay width for  $D_s^+ \rightarrow \tau^+ \nu$ , where  $\tau^+ \rightarrow e^+ \nu \bar{\nu}$ .

In the Standard Model (SM) these decays are described by the annihilation of the initial quark-antiquark pair into a virtual  $W^+$  that materializes as a  $\ell^+ \nu$  pair; the process is shown in Fig. 1. The decay rate is given by [3]

$$\Gamma(D_s^+ \rightarrow \ell^+ \nu) = \frac{G_F^2}{8\pi} f_{D_s^+}^2 m_\ell^2 M_{D_s^+} \left(1 - \frac{m_\ell^2}{M_{D_s^+}^2}\right)^2 |V_{cs}|^2 \quad , \quad (1)$$

where  $M_{D_s^+}$  is the  $D_s^+$  mass,  $m_\ell$  is the mass of the charged final state lepton,  $G_F$  is the Fermi coupling constant, and  $|V_{cs}|$  is a Cabibbo-Kobayashi-Maskawa matrix element with a value we take equal to  $|V_{ud}|$  of 0.97418(26) [4], and  $f_{D_s^+}$  is the ‘‘decay constant,’’ a parameter related to the overlap of the heavy and light quark wave-functions at zero spatial separation.

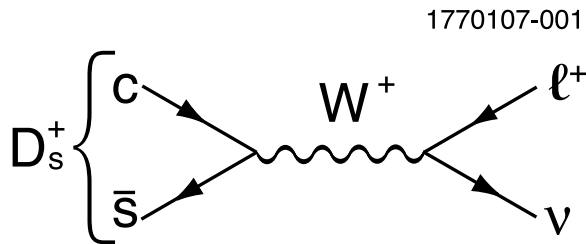


FIG. 1: The decay diagram for  $D_s^+ \rightarrow \ell^+ \nu$ .

The SM decay rate then is predicted using a theoretical calculation of the decay constant. Two calculations have been carried out using unquenched lattice quantum-chromodynamics (LQCD). Aubin *et al.* find  $f_{D_s^+} = (249 \pm 3 \pm 16)$  MeV [5], while a more recent calculation of Follana *et al.* gives  $(241 \pm 3)$  MeV [6]. The latter calculation is more than three standard deviations lower than the average of previous CLEO and Belle measurements [7].

Dobrescu and Kronfeld have proposed three models based on physics beyond the SM that are consistent with known data and could possibly explain the difference. One is a charged Higgs model and the other two involve different manifestations of leptoquarks [8]. The recent CLEO measurement of  $f_{D^+} = (205.8 \pm 8.5 \pm 2.5)$  MeV, is consistent with both the Aubin *et al.* and Follana *et al.* predictions, of  $(201 \pm 3 \pm 17)$  MeV and  $(208 \pm 4)$  MeV, respectively [9].

It is particularly important to understand if the discrepancy in the  $D_s$  case is due to physics beyond the SM, a faulty theoretical calculation, or to an unlikely measurement fluctuation. We note that precise information on the size of Cabibbo-Kobayashi-Maskawa matrix elements extracted from  $B - \bar{B}$  mixing measurements requires theoretical input on the ‘‘decay constants’’ for  $B_d$  and  $B_s$  mesons or their ratio,  $f_{B_s}/f_{B_d}$  [10]. Although the calculations in the  $B$  and  $D$  systems are not the same, many of the techniques used are common, and a discrepancy in the charm system at a minimum, does not give confidence in the theoretical predictions for the  $B$  system. In this paper we present an updated measurement of  $f_{D_s^+}$  with much improved precision.

Akeroyd predicts that the presence of a charged Higgs boson would suppress  $f_{D_s}$  [11]. There is however the possibility, not considered by Akeroyd, that it is the charm quark that is responsible for a NP contribution not the  $s$  quark [8]. In that case the relative change would be similar in  $D^+$  and  $D_s^+$  decays.

We can also measure the ratio of decay rates to different leptons, and the SM predictions then are fixed only by well-known masses. For example, for  $\tau^+\nu$  to  $\mu^+\nu$ :

$$R \equiv \frac{\Gamma(D_s^+ \rightarrow \tau^+\nu)}{\Gamma(D_s^+ \rightarrow \mu^+\nu)} = \frac{m_{\tau^+}^2 \left(1 - \frac{m_{\tau^+}^2}{M_{D_s^+}^2}\right)^2}{m_{\mu^+}^2 \left(1 - \frac{m_{\mu^+}^2}{M_{D_s^+}^2}\right)^2} . \quad (2)$$

Using measured masses [12], this expression yields a value of 9.76 with a small error. Any deviation in  $R$  from the value predicted by Eq. (2) would be a manifestation of physics beyond the SM. This could occur if any other charged intermediate boson existed that affected the decay rate differently than mass-squared. Then the couplings would be different for muons and  $\tau$ 's. This would be a clear violation of lepton universality [13].

Most other measurements of  $f_{D_s^+}$  have been hampered by a lack of statistical precision, and relatively large systematic errors [14–19]. One large systematic error source has been the lack of knowledge of the absolute branching fraction of the normalization channel, usually  $D_s^+ \rightarrow \phi\pi^+$  [20]. The results we report here will not have this limitation, nor did our previous measurement [1], nor did the Belle measurement [21].

In both  $\mu^+\nu$  and  $\tau^+\nu$   $D_s$  decays the charged lepton must be produced with the wrong helicity because the  $D_s$  is a spin-0 particle, and the final state consists of a naturally left-handed spin-1/2 neutrino and a naturally right-handed spin-1/2 anti-lepton. Because the  $\tau^+$  has a mass close to that of the  $D_s^+$ , the helicity suppression is broken with respect to the  $\mu^+$  decay, but there is an additional large phase space suppression. Because of the helicity suppression in  $\mu^+\nu$  the radiative process  $\gamma\mu^+\nu$  may have a significant rate. Dobrescu and Kronfeld, however, estimate this process is only 1% of the lowest order mechanism, for photon momenta below 300 MeV, which is relevant range for this analysis. We include this radiative correction in what follows [8, 22]. (There is no correction for the  $\tau^+\nu$  final state.) The data will also be corrected for final state radiation of the muon, as our Monte Carlo simulation incorporates this effect [23].

## II. EXPERIMENTAL METHOD

### A. Selection of $D_s$ Candidates

The CLEO-c detector [24] is equipped to measure the momenta and directions of charged particles, identify them using specific ionization ( $dE/dx$ ) and Cherenkov light (RICH) [25], detect photons and determine their directions and energies.

In this study we use 600 pb<sup>-1</sup> of data produced in  $e^+e^-$  collisions using the Cornell Electron Storage Ring (CESR) and recorded near a center-of-mass energy ( $E_{\text{CM}}$ ) of 4.170 GeV. At this energy the  $e^+e^-$  annihilation cross-section into  $D_s^-D_s^{*+} + D_s^{*-}D_s^+$  is approximately 1 nb, while the cross-section for  $D_s^+D_s^-$  is about a factor of 20 smaller. In addition,  $D$  mesons are produced mostly as  $D^*\bar{D}^*$ , with a cross-section of  $\sim 5$  nb, and also in  $D^*\bar{D} + D\bar{D}^*$  final

states with a cross-section of  $\sim 2$  nb. The  $D\bar{D}$  cross-section is a relatively small  $\sim 0.2$  nb [26]. There also appears to be  $D\bar{D}^*\pi$  production. The underlying light quark “continuum” background is about 12 nb. The relatively large cross-sections, relatively large branching fractions, and sufficient luminosities allow us to fully reconstruct one  $D_s$  as a “tag,” and examine the properties of the other. In this paper we designate the tag as a  $D_s^-$  and examine the leptonic decays of the  $D_s^+$ , though in reality we use both charges for tags and signals. Track requirements, particle identification,  $\pi^0$ ,  $\eta$ , and  $K_S^0$  selection criteria are the same as those described in Ref. [27], except that we now require a minimum momentum of 700 MeV/c for a track to be identified using the RICH.

We also use several resonances that decay via the strong interaction. Here we select intervals in invariant mass within  $\pm 10$  MeV of the known mass for  $\eta' \rightarrow \pi^+\pi^-\eta$ ,  $\pm 20$  MeV of the known mass for  $\eta' \rightarrow \rho^0\gamma$ ,  $\pm 10$  MeV for  $\phi \rightarrow K^+K^-$ ,  $\pm 100$  MeV for  $K^{*0} \rightarrow K^-\pi^+$ , and  $\pm 150$  MeV for  $\rho^- \rightarrow \pi^-\pi^0$  or  $\rho^0 \rightarrow \pi^+\pi^-$ .

We reconstruct tags from either directly produced  $D_s$  mesons or those that result from the decay of a  $D_s^*$ . The beam constrained mass,  $m_{\text{BC}}$ , is formed by using the beam energy to construct the  $D_s$  candidate mass via the formula

$$m_{\text{BC}} = \sqrt{E_{\text{beam}}^2 - \left(\sum_i \mathbf{p}_i\right)^2}, \quad (3)$$

where  $i$  runs over all the final state particles. If we ignore the photon from the  $D_s^* \rightarrow \gamma D_s$  decay, and reconstruct the  $m_{\text{BC}}$  distribution, we obtain the distribution from Monte Carlo simulation shown in Fig. 2. The narrow peak occurs when the reconstructed  $D_s$  does not come from the  $D_s^*$  decay, but is directly produced.

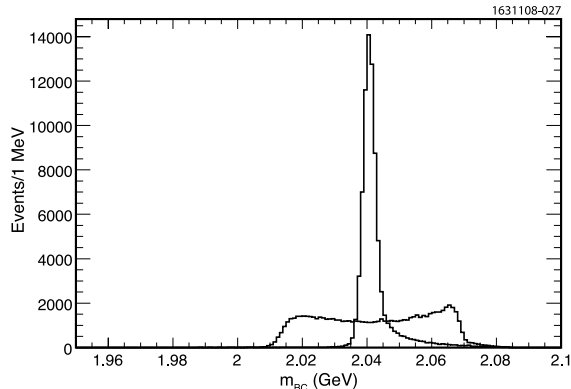


FIG. 2: The beam constrained mass  $m_{\text{BC}}$  from Monte Carlo simulation of  $e^+e^- \rightarrow D_s^+ D_s^{*-}$  at an  $E_{\text{CM}}$  of 4170 MeV. The narrow peak is from the  $D_s^+$  and the wider one from  $D_s^{*-} \rightarrow \gamma D_s^-$ . (The distributions are not centered at the  $D_s^+$  or  $D_s^{*+}$  masses, because the reconstructed particles are assumed to have the energy of the beam.)

Rather than selecting events based on only  $m_{\text{BC}}$ , we first select an interval that accepts most of the events,  $2.015 < m_{\text{BC}} < 2.067$  GeV, and examine the invariant mass. Distributions from data for the nine tag decay modes we use in this analysis are shown in Fig. 3. Note that the resolution in invariant mass is excellent, and the backgrounds not abysmally large, at least in these modes. To determine the number of  $D_s^-$  events we fit the invariant mass

distributions to the sum of two Gaussians centered at the  $D_s^-$  mass, a function we refer to as “two-Gaussian.” The r.m.s. resolution ( $\sigma$ ) is defined as

$$\sigma \equiv f_1\sigma_1 + (1 - f_1)\sigma_2, \quad (4)$$

where  $\sigma_1$  and  $\sigma_2$  are the individual widths of each of the two Gaussians and  $f_1$  is the fractional area of the first Gaussian. The number of tags in each mode is listed in Table I. There are two changes in modes from our previous analysis [1]; instead of  $\phi\rho^-$ , we now use  $K^+K^-\pi^-\pi^0$ , and we have added the  $\eta'\pi^-$ ,  $\eta' \rightarrow \rho^0\gamma$  mode; the background here is somewhat reduced as we apply a cut on the helicity angle,  $\theta$  of  $|\cos\theta| < 0.8$ , since the  $\rho^0$  is polarized as  $\sin^2\theta$ . (Here  $\theta$  is the angle of the  $\pi^+$  in the  $\rho^0$  rest frame with respect to the  $\rho^0$  direction in the parent frame.) These changes results in an increase of 20% more tags at the expense of more background.

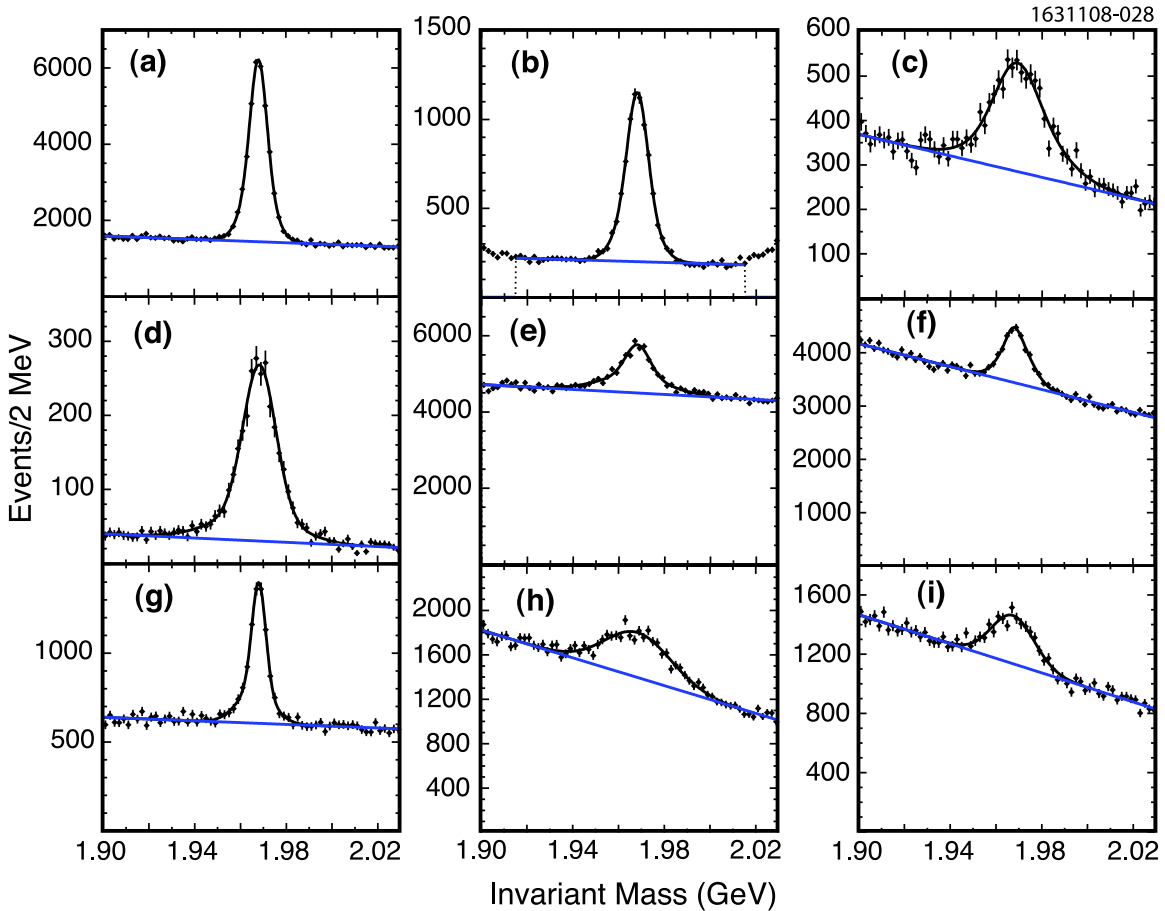


FIG. 3: Invariant mass of  $D_s^-$  candidates in the decay modes (a)  $K^+K^-\pi^-$ , (b)  $K_S K^-$ , (c)  $\eta\pi^-$  ( $\eta \rightarrow \gamma\gamma$ ), (d)  $\eta'\pi^-$  ( $\eta' \rightarrow \pi^+\pi^-\eta$ ,  $\eta \rightarrow \gamma\gamma$ ) (e)  $K^+K^-\pi^-\pi^0$  (f)  $\pi^+\pi^-\pi^-$ , (g)  $K^{*-}K^{*0}$ ,  $K^{*-} \rightarrow K_S^0\pi^-$  ( $K^{*0} \rightarrow K^+\pi^-$ ), (h)  $\eta\rho^-$ , and (i)  $\eta'\pi^-$  ( $\eta' \rightarrow \rho^0\gamma$ ), after requiring the total energy of the  $D_s^-$  candidate to be consistent with the beam energy. The curves are fits to two-Gaussian signal functions plus a linear background. The dashed vertical lines in (b) indicate the restricted fit region.

TABLE I: Tagging modes and numbers of signal and background events, within  $\pm 17.5$  MeV of the  $D_s^-$  mass for each mode, determined from two-Gaussian fits to the invariant mass plots, and the number of tags in each mode including the  $\gamma$  from the  $D_s^* \rightarrow \gamma D_s$  transition, within an interval  $3.872 < \text{MM}^{*2} < 4.0 \text{ GeV}^2$ , as determined from fits of the  $\text{MM}^{*2}$  distributions (see text) to a signal Crystal Ball function (see text) and two 5th order Chebychev background polynomials.

Mode	Invariant Mass		$\text{MM}^{*2}$	
	Signal	Background	Signal	Background
$K^+ K^- \pi^-$	26534 $\pm$ 274	25122	16087 $\pm$ 373	39563
$K_S K^-$	6383 $\pm$ 121	3501	4215 $\pm$ 228	6297
$\eta \pi^-; \eta \rightarrow \gamma \gamma$	2993 $\pm$ 156	5050	2005 $\pm$ 145	5016
$\eta' \pi^-; \eta' \rightarrow \pi^+ \pi^- \eta, \eta \rightarrow \gamma \gamma$	2293 $\pm$ 82	531	1647 $\pm$ 131	1565
$K^+ K^- \pi^- \pi^0$	11649 $\pm$ 754	78588	6441 $\pm$ 471	89284
$\pi^+ \pi^- \pi^-$	7374 $\pm$ 303	60321	5014 $\pm$ 402	43286
$K^{*-} K^{*0}; K^{*-} \rightarrow K_S^0 \pi^-, K^{*0} \rightarrow K^+ \pi^-$	4037 $\pm$ 160	10568	2352 $\pm$ 176	12088
$\eta \rho^-; \eta \rightarrow \gamma \gamma, \rho^- \rightarrow \pi^- \pi^0$	5700 $\pm$ 281	24444	3295 $\pm$ 425	24114
$\eta' \pi^-; \eta' \rightarrow \rho^0 \gamma,$	3551 $\pm$ 202	19841	2802 $\pm$ 227	17006
Sum	70514 $\pm$ 963	227966	43859 $\pm$ 936	238218

We list the number of signal events in each mode in Table I by finding the number of events within  $\pm 17.5$  MeV of the  $D_s$  mass; here we integrate the two-Gaussian PDF over the interval. We also include the amount of background in this interval. For ease of further analysis we sum all tag modes together, as shown in Fig. 4.

In this analysis we look for two types of events: (1)  $e^+ e^- \rightarrow D_s^{*-} D_s^+$ , and (2)  $e^+ e^- \rightarrow D_s^- D_s^{*+}$ , where our convention is that the tag is denoted by the negative charge state and the putative signal  $\mu^+ \nu$  decay by the positive charge state. Thus, we need to detect the photon from the  $D_s^*$  decay. Therefore, we look for an additional photon candidate in the event that satisfies our shower shape requirement. Regardless of whether or not the photon forms a  $D_s^*$  with the tag, for real  $D_s^* D_s$  events, the missing mass squared,  $\text{MM}^{*2}$ , recoiling against the photon and the  $D_s^-$  tag should peak at the  $D_s^+$  mass-squared. We calculate

$$\text{MM}^{*2} = (E_{\text{CM}} - E_{D_s} - E_\gamma)^2 - (\mathbf{p}_{\text{CM}} - \mathbf{p}_{D_s} - \mathbf{p}_\gamma)^2, \quad (5)$$

where  $E_{\text{CM}}$  ( $\mathbf{p}_{\text{CM}}$ ) is the center-of-mass energy (momentum),  $E_{D_s}$  ( $\mathbf{p}_{D_s}$ ) is the energy (momentum) of the fully reconstructed  $D_s^-$  tag, and  $E_\gamma$  ( $\mathbf{p}_\gamma$ ) is the energy (momentum) of the additional photon. In performing this calculation we use a kinematic fit that constrains the decay products of the  $D_s^-$  to the known  $D_s$  mass and conserves overall momentum and energy. All photon candidates in the event are used, except for those that are decay products of the  $D_s^-$  tag candidate.

The  $\text{MM}^{*2}$  distributions for events in the  $D_s^-$  invariant mass signal region ( $\pm 17.5$  MeV from the  $D_s$  mass) are shown in Fig. 5. In order to find the number of tags used for further analysis we perform a two-dimensional binned maximum likelihood fit of the  $\text{MM}^{*2}$  distribution and the invariant mass distribution in the interval  $\pm 60$  MeV from the  $D_s$  mass and  $3.5 < \text{MM}^{*2} < 4.25 \text{ GeV}^2$ . This procedure is improved by having information on the shape of the  $\text{MM}^{*2}$  signal function (often called a Probability Distribution Function,

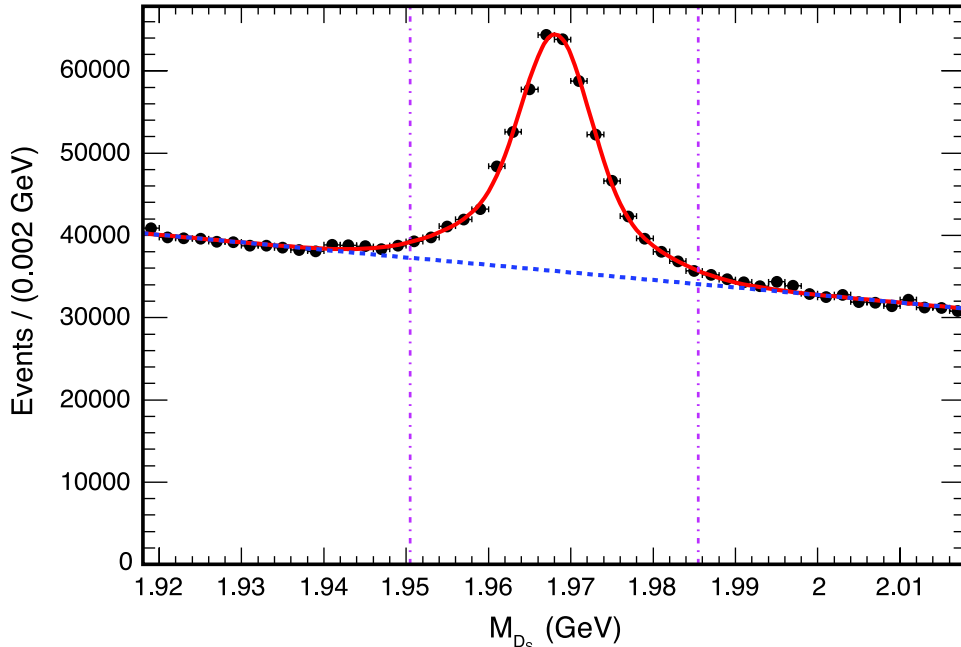


FIG. 4: Invariant mass of  $D_s^-$  candidates summed over all decay modes and fit to a two-Gaussian signal shape plus a straight line for the background. The vertical dot-dashed lines indicate the  $\pm 17.5$  MeV definition of the signal region.

or PDF). One possibility is to use the Monte Carlo simulation for this purpose, but that would introduce a relatively large systematic uncertainty. Instead, we use our relatively large sample of fully reconstructed  $D_s D_s^*$  events, where we use the same decay modes listed in Table I; we find these events and then examine the signal shape in data when one  $D_s$  is ignored.

To remove background we subtract invariant mass sidebands. Some random photon background remains. We remove this by examining the direction of the candidate photon; it should be opposite the direction of the  $D_s^+ D_s^-$  system for signal. Defining the angle  $\theta_\gamma$  to be that between the three-vector of the candidate photon and the  $D_s^+ D_s^-$  system, we require that  $-1.0 < \cos(\theta_\gamma) < -0.95$ . Furthermore we use the events for  $-0.8 < \cos(\theta_\gamma) < 1.0$  as background and subtract them also. The  $MM^{*2}$  distribution from this sample is shown in Fig. 6. The signal is fit to a Crystal Ball function [28, 29]. The  $\sigma$  parameter, that represents the width of the distribution, is found to be  $0.035 \pm 0.001$  GeV<sup>2</sup>. We do expect this to vary somewhat depending on the final state, but we do not expect the parameters that fix the shape of the tail to change, since they depend mostly on initial state radiation, beam energy spread, and the properties of photon detection.

The background has two components, both described by 5th order Chebyshev polynomials; the first comes from the background under the invariant mass peak, defined by the sidebands, and the second is due to multiple photon combinations. In both cases we allow the parameters to float.

We find a total of  $43859 \pm 936$  events within within the interval  $3.872 < MM^{*2} < 4.0$  GeV<sup>2</sup> and having an invariant mass within  $\pm 17.5$  MeV of the  $D_s$  mass, where the total number of events is the sum of the yields from the fits to each mode as shown in Table I. An overall

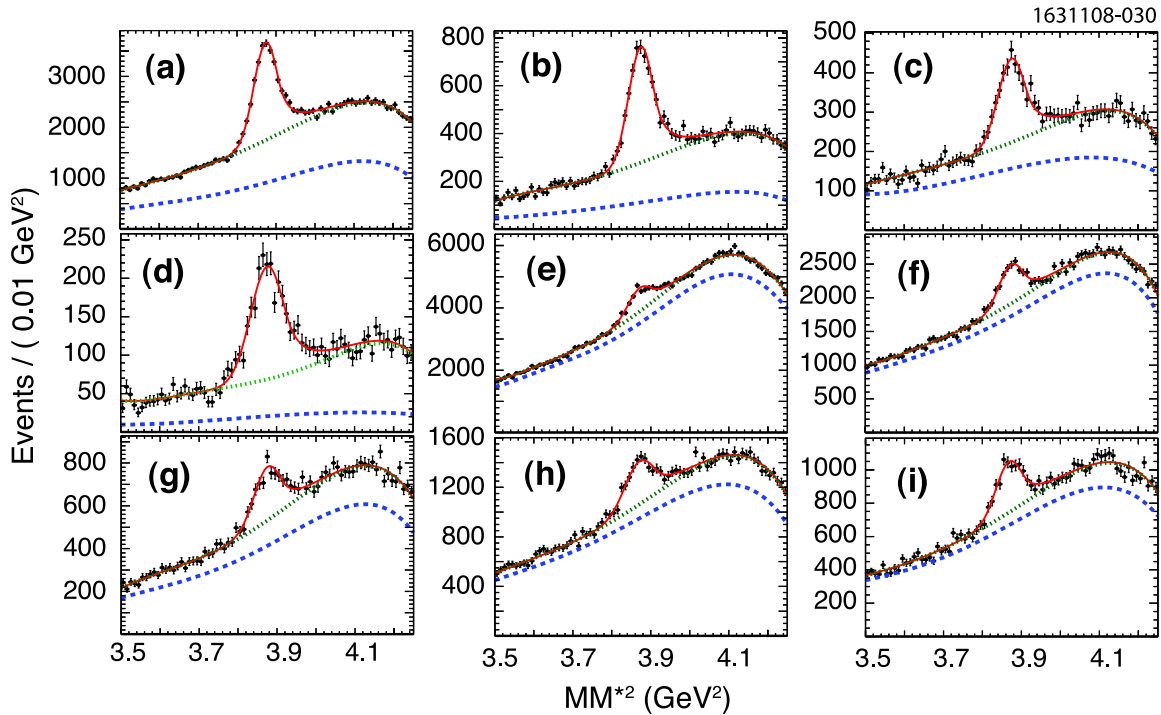


FIG. 5: The  $MM^{*2}$  distribution from events with a photon in addition to the  $D_s^-$  tag for the modes: (a)  $K^+K^-\pi^-$ , (b)  $K_S^0K^-$ , (c)  $\eta\pi^-$ , (d)  $\eta'\pi^-$ , (e)  $K^+K^-\pi^-\pi^0$ , (f)  $\pi^+\pi^-\pi^-$ , (g)  $K^{*-}K^{*0}$ , (h)  $\eta\rho^-$ , and (i)  $\eta'\pi^-$ ,  $\eta' \rightarrow \pi^+\pi^-\gamma$ . The curves are fits to Crystal Ball functions and two 5th order Chebychev background functions (see text).

systematic error of 2.0% on the number of tags is assigned by using different functions for the description of the backgrounds. If we fix the shape of the multiple photon combinations background polynomial to that given by the Monte Carlo, we increase the yield by 1.1%. If we use a 4th order polynomial to describe the background of non- $D_s^-$  events, we decrease the yield by 1.6%; on the other hand using a 6th order polynomial increases the yield by 1.7%. Combining the results of changing both background shapes in quadrature for the worst case, we assign a systematic error of  $\pm 2.0\%$  on the tag yield.

We also determine the number of  $D_s^-$  tags when the tag results from the decay  $D_s^{*-} \rightarrow \gamma D_s^-$ . This procedure reduces the background considerably in determining the tag yield and results in counting half of the tags. Adopting this procedure we find a tag yield that is higher by  $(1.2 \pm 2.3)\%$  from our nominal procedure, consistent with the assigned systematic error. The summed  $MM^{*2}$  distribution is shown in Fig. 7.

There is also a small enhancement of 5.2% in our ability to find tags in  $\mu^+\nu$  (or  $\tau^+\nu$ ,  $\tau^+ \rightarrow \pi^+\bar{\nu}$ ) events (tag bias) as compared with events where the  $D_s^+$  decays generically. We determine this correction by using a Monte Carlo simulation for each tag mode independently and then average the results based on the known tag fractions. We assign a systematic error of 20% giving a correction of  $(5.2 \pm 1.0)\%$ .

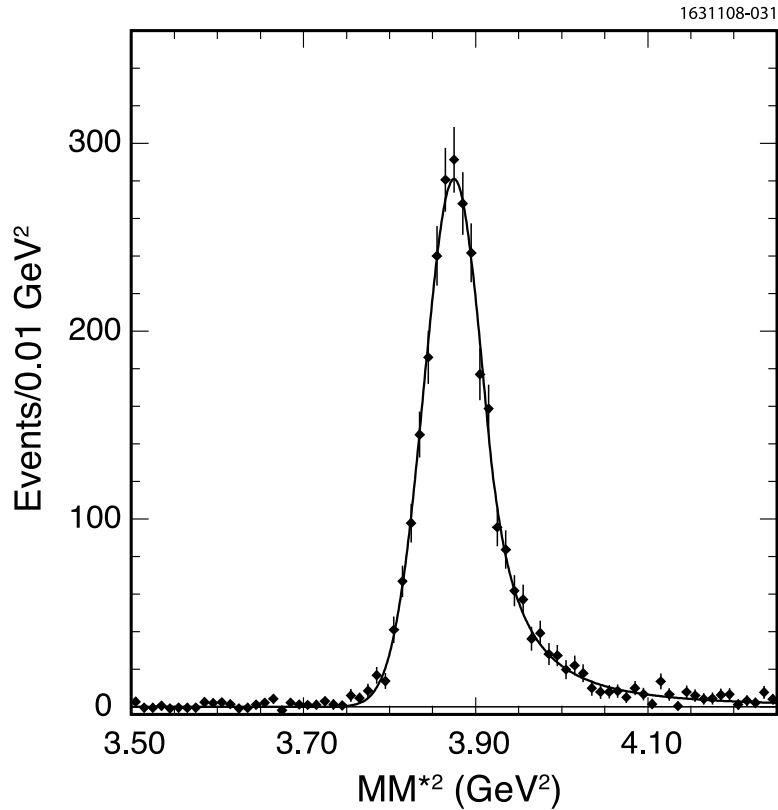


FIG. 6: The  $MM^{*2}$  distribution from a sample of fully reconstructed  $D_s^- D_s^{*+}$  and  $D_s^{*-} D_s^+$  events where one  $D_s$  is ignored. The curve is a fit to the Crystal Ball function.

## B. Signal Reconstruction

We next describe the search for  $D_s^+ \rightarrow \mu^+ \nu$ . We select events within the  $MM^{*2}$  region shown in Fig. 7 for further analysis. We note that the limits are rather wide. We use this selection because the background in the signal side is rather small and the errors are minimized by taking as many tags as possible.

Candidate events are selected that contain only a single extra track with opposite charge to the tag. The track must make an angle  $>25.8^\circ$  with respect to the beam line to ensure that it is well measured, and in addition we require that there not be any neutral cluster detected in the calorimeter, not associated with the tag, with energy greater than 300 MeV (photon veto). These cuts are highly effective in reducing backgrounds. The photon energy cut is especially useful to reject  $D_s^+ \rightarrow \pi^+ \pi^0$ , should this mode be significant, and  $D_s^+ \rightarrow \eta \pi^+$ .

Since we are searching for events where there is a single missing neutrino, the missing mass squared,  $MM^2$ , evaluated by taking into account the observed  $\mu^+$ ,  $D_s^-$ , and  $\gamma$  should peak at zero; the  $MM^2$  is computed as

$$MM^2 = (E_{\text{CM}} - E_{D_s} - E_\gamma - E_\mu)^2 - (\mathbf{p}_{\text{CM}} - \mathbf{p}_{D_s} - \mathbf{p}_\gamma - \mathbf{p}_\mu)^2, \quad (6)$$

where  $E_\mu$  ( $\mathbf{p}_\mu$ ) are the energy (momentum) of the candidate muon track and all other variables are the same as defined in Eq. (5).

We also make use of a set of kinematical constraints and fit each event to two hypotheses

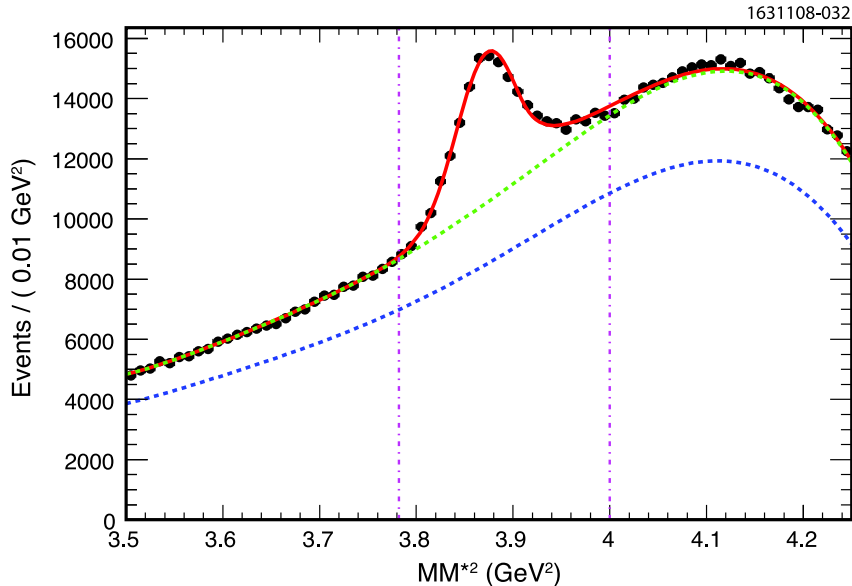


FIG. 7: The  $MM^2$  distribution summed over all modes. The curves are fits to the number of signal events using the Crystal Ball function and two 5th order Chebychev background functions (see text). The vertical lines show the region of events selected for further analysis.

one of which is that the  $D_s^-$  tag is the daughter of a  $D_s^{*-}$  and the other that the  $D_s^{*+}$  decays into  $\gamma D_s^+$ , with the  $D_s^+$  subsequently decaying into  $\mu^+\nu$ . The kinematical constraints, in the  $e^+e^-$  center-of-mass frame, are

$$\begin{aligned}
 \mathbf{p}_{D_s} + \mathbf{p}_{D_s^*} &= 0 & (7) \\
 E_{\text{CM}} &= E_{D_s} + E_{D_s^*} \\
 E_{D_s^*} &= \frac{E_{\text{CM}}}{2} + \frac{M_{D_s^*}^2 - M_{D_s}^2}{2E_{\text{CM}}} \text{ or } E_{D_s} = \frac{E_{\text{CM}}}{2} - \frac{M_{D_s^*}^2 - M_{D_s}^2}{2E_{\text{CM}}} \\
 M_{D_s^*} - M_{D_s} &= 143.8 \text{ MeV}.
 \end{aligned}$$

In addition, we constrain the invariant mass of the  $D_s^-$  tag to the known  $D_s$  mass. This gives us a total of 7 constraints. The missing neutrino four-vector needs to be determined, so we are left with a three-constraint fit. We perform a standard iterative fit minimizing  $\chi^2$ . As we do not want to be subject to systematic uncertainties that depend on understanding the absolute scale of the errors, we do not make a  $\chi^2$  cut but simply choose the photon and the decay sequence in each event with the minimum  $\chi^2$ .

In this analysis, we consider three separate cases: (i) the track deposits  $< 300$  MeV in the calorimeter, characteristic of a non-interacting pion or a muon; (ii) the track deposits  $> 300$  MeV in the calorimeter, characteristic of an interacting pion, and is not consistent with being an electron; (iii) the track satisfies our electron selection criteria; for a track to be called an electron, we require that the momentum measurement in the tracking system and the energy deposited in the CsI calorimeter are close to being equal within errors, and we also require that  $dE/dx$  and RICH information be consistent with expectations for an electron. Then we separately study the  $MM^2$  distributions for these three cases. The separation between muons and pions is not complete. Case (i) contains 98.8% of the muons but also 55% of the

pions, while case (ii) includes 1.2% of the muons and 45% of the pions [30]. Case (iii) does not include any signal but is used later to search for  $D_s^+ \rightarrow e^+\nu$ . For cases (i) and (ii) we insist that the track not be identified as a kaon.

### C. The Expected $MM^2$ Signal Spectrum

For the  $\mu^+\nu$  final state the  $MM^2$  distribution can be modeled as the sum of two Gaussians centered at zero (see Eq. (4)). A Monte Carlo simulation of the  $MM^2$  is shown in Fig. 8. A fit using the two-Gaussian shape gives  $\sigma_1 = 0.0240 \text{ GeV}^2$ ,  $\sigma_2 = 0.0851 \text{ GeV}^2$ ,  $f = 0.275$ , which results in  $\sigma = 0.0346 \pm 0.0002 \text{ GeV}^2$ .

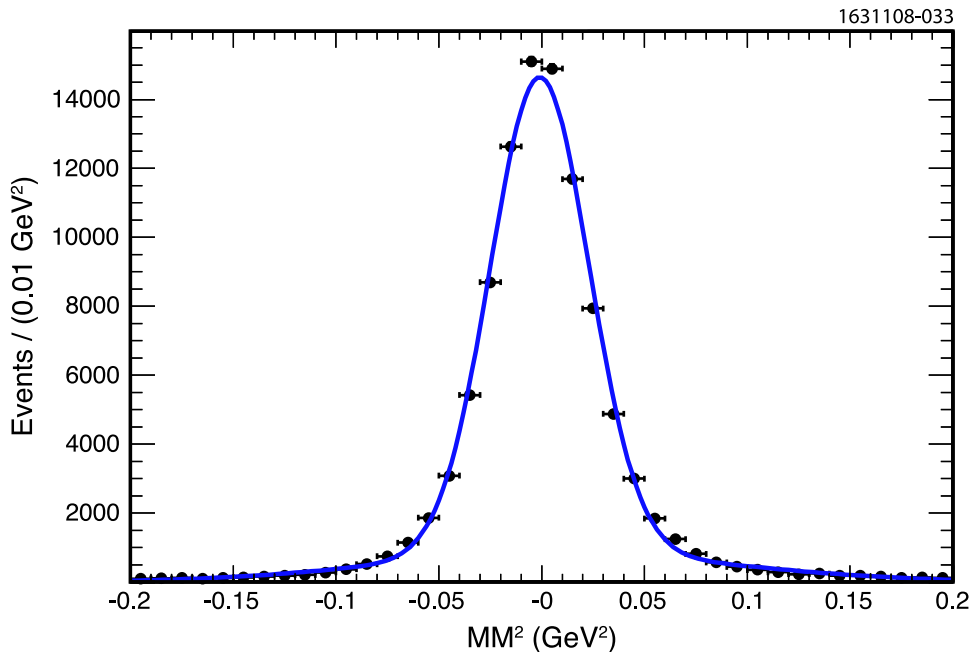


FIG. 8: The  $MM^2$  resolution from Monte Carlo simulation for  $D_s^+ \rightarrow \mu^+\nu$ . The curve is the sum of two-Gaussians with means constrained to be the same.

We check the resolution using data. The mode  $D_s^+ \rightarrow \bar{K}^0 K^+$  provides an excellent testing ground.<sup>1</sup> We search for events with at least one additional track identified as a kaon using the RICH detector, in addition to a  $D_s^-$  tag. We allow events with no more than two other additional charged tracks, to allow for the presence of  $K^0$  decays, and we do not apply the greater than 300 MeV extra energy cut. The  $MM^2$  distribution is shown in Fig. 9. Fitting this distribution to a two-Gaussian signal shape gives a  $MM^2$  resolution  $\sigma = 0.0338 \pm 0.0014 \text{ GeV}^2$  in agreement with Monte Carlo simulation which gives  $0.0344 \pm 0.0003 \text{ GeV}^2$ . (The backgrounds are discussed in section IV.) We note that the resolution here is larger than in our previous work [1]. This is mainly due to the use of additional decay modes with photons, and enlarging of the solid angle for candidate muons.

<sup>1</sup> In this paper the notation  $\bar{K}^0 K^+$  refers to the sum of  $\bar{K}^0 K^+$  and  $K^0 K^+$  final states.

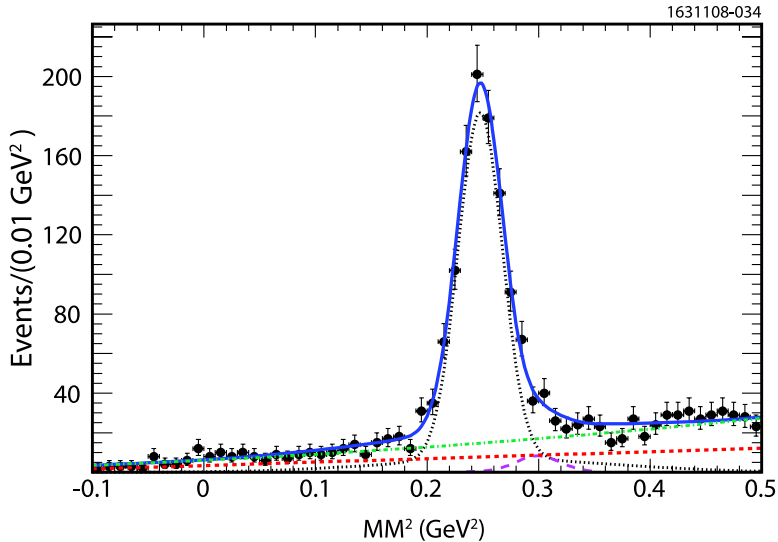


FIG. 9: The  $MM^2$  distribution for events with an identified  $K^+$  track. The kinematic fit has been applied. The data are shown as points with error bars. The long-dashed curve shows the calculated yield of  $\eta K^+$  events. The solid curve shows the results of a fit to the data, where the dotted curve is the sum of two Gaussians centered at the square of the  $K^0$  mass, and the dashed and dot-dashed lines refer to the sideband, and combinatoric backgrounds, respectively.

For the  $\tau^+\nu$ ,  $\tau^+ \rightarrow \pi^+\bar{\nu}$  final state a Monte Carlo simulation of the  $MM^2$  spectrum is shown in Fig. 10. The extra missing neutrino results in a smeared distribution.

#### D. $MM^2$ Spectra in Data

The  $MM^2$  distributions from data are shown in Fig. 11. The overall signal region we consider is  $-0.1 < MM^2 < 0.20 \text{ GeV}^2$ . The higher limit is imposed to exclude background from  $\eta\pi^+$  and  $K^0\pi^+$  final states. There is a clear peak in Fig. 11(a) due to  $D_s^+ \rightarrow \mu^+\nu$ . Furthermore, the region between the  $\mu^+\nu$  peak and  $0.20 \text{ GeV}^2$  has events that we will show are mainly due to the  $D_s^+ \rightarrow \tau^+\nu$ ,  $\tau^+ \rightarrow \pi^+\bar{\nu}$  decay. The events in Fig. 11(b) below  $0.20 \text{ GeV}^2$  are also mostly due to  $\tau^+\nu$  decay.

#### E. Background Evaluations

We consider the background arising from two sources: one from real  $D_s^+$  decays and the other from the background under the single-tag signal peaks. For the latter, we obtain the background from data by using a two-dimensional extended likelihood fit in invariant mass and  $MM^2$ .

The background from real  $D_s^+$  decays is studied by identifying each possible source mode by mode. For the  $\mu^+\nu$  final state, the only possible background within the signal region is  $D_s^+ \rightarrow \pi^+\pi^0$ . (Recall that any such events are also heavily suppressed by the extra photon energy veto of 300 MeV.) We search for this mode by examining the  $\pi^+\pi^0$  invariant mass spectrum in events where we have selected a  $D_s^-$  tag based on invariant mass only. See

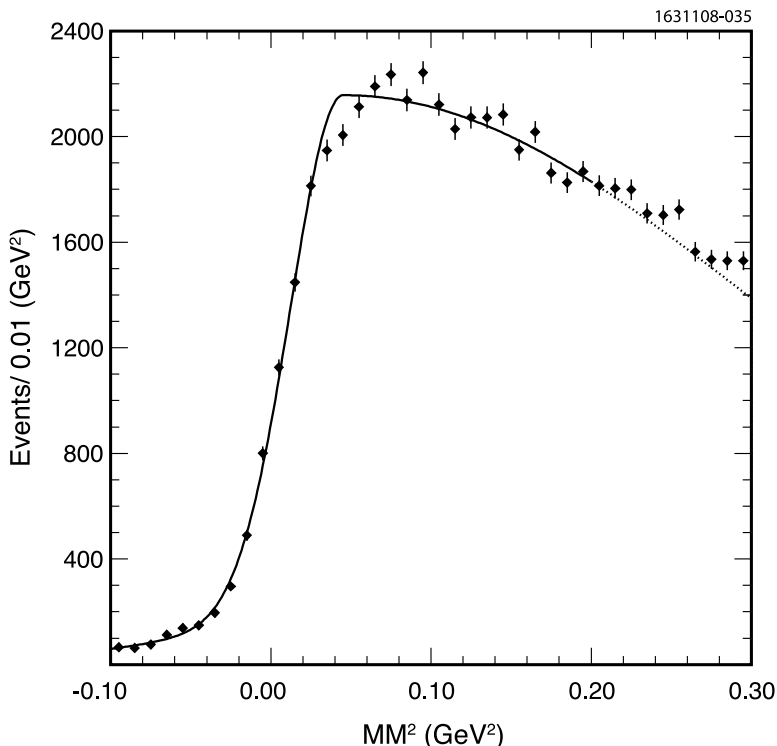


FIG. 10: The  $MM^2$  distribution from Monte-Carlo simulation for  $D_s^+ \rightarrow \tau^+\nu$ ,  $\tau^+ \rightarrow \pi^+\bar{\nu}$  at an  $E_{\text{CM}}$  of 4170 MeV. The curve is a fit to the sum of two-Gaussians with different widths on the low and high  $MM^2$  sides.

Fig. 12. There is no peak at the  $D_s^+$  mass. Fitting to a linear background plus a Crystal-Ball signal function, whose shape is fixed by Monte Carlo gives  $-3.6 \pm 8.4$  events. Setting the mean value to zero results in an upper limit  $\mathcal{B}(D_s^+ \rightarrow \pi^+\pi^0) < 3.8 \times 10^{-4}$  at 90% confidence level. Multiplying by our 43859 tags and the 2% inefficiency for detecting a  $> 300$  MeV photon from the  $\pi^0$  decays, results in an upper limit of 1/4 of an event in our sample, which we ignore.

For the  $\tau^+\nu$ ,  $\tau^+ \rightarrow \pi^+\bar{\nu}$  final state the real  $D_s^+$  backgrounds include, in addition to the  $\pi^+\pi^0$  background discussed above, semileptonic decays, possible  $\pi^+\pi^0\pi^0$  decays, other  $\tau^+$  decays, and small amounts of  $K^0\pi^+$  and  $\eta\pi^+$  whose low  $MM^2$  tails leak into the signal region. Semileptonic decays involving muons are equal to those involving electrons shown in Fig. 11(c). One event consistent with the electron hypothesis is present. The  $\pi^+\pi^0\pi^0$  background level is estimated by considering the  $\pi^+\pi^+\pi^-$  final state whose measured branching fraction is  $(1.11 \pm 0.07 \pm 0.04)\%$  [31]. This mode has large contributions from  $f_0(980)\pi^+$  and other  $\pi^+\pi^-$  resonant structures at higher mass [32]. The  $\pi^+\pi^0\pi^0$  mode will also have these contributions, but the  $MM^2$  opposite to the  $\pi^+$  will be at large mass. The only component that can potentially cause background is the non-resonant component measured by FOCUS as  $(17 \pm 4)\%$  [32]. This background has been evaluated by Monte Carlo simulation as have backgrounds from other  $\tau^+$  decays,  $K^0\pi^+$  and  $\eta\pi^+$ . The backgrounds are enumerated in Table II. We show in Fig. 13 the sum of all backgrounds and a fit to a quadratic polynomial over the  $MM^2$  range of interest.

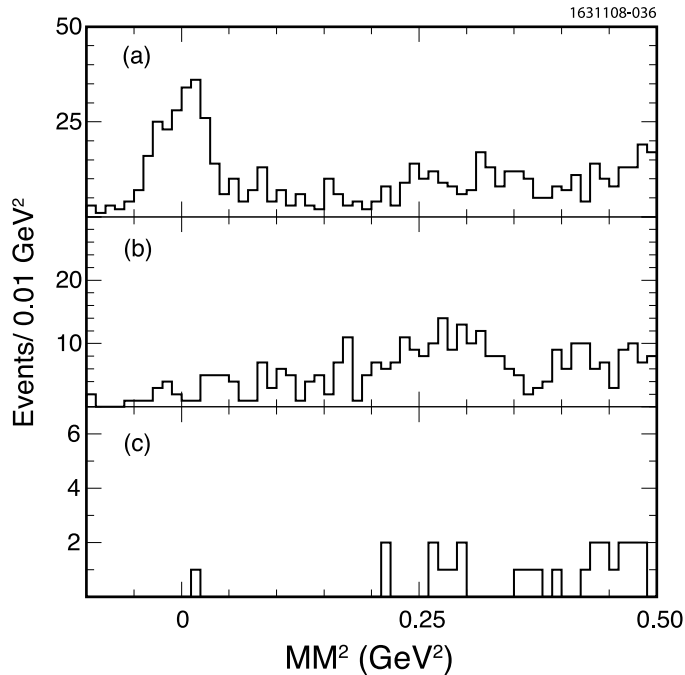


FIG. 11: The  $MM^2$  distributions from data for events with a  $D_s^-$  reconstructed in a tag mode, an additional positively charged track and no neutral energy clusters above 300 MeV. (a) Case (i) when the single track deposits  $< 300$  MeV of energy in the calorimeter. The peak near zero is from  $D_s^+ \rightarrow \mu^+\nu$  events. (b) Case (ii): the track deposits  $> 300$  MeV in the crystal calorimeter but is not consistent with being an electron. (c) Case (iii): the track is identified as an electron.

TABLE II: Background estimates for the data in the signal region  $-0.1 < MM^2 < 0.2$  GeV<sup>2</sup>. (We assume  $\mathcal{B}(D_s^+ \rightarrow \tau^+\nu) = 6.2 \pm 0.7\%$ .)

Final State	$\mathcal{B}(\%)$	# of events case(i)	# of events case (ii)
$\tau^+ \rightarrow \pi^+\pi^0\bar{\nu}$	$1.6 \pm 0.2$	$2.06 \pm 0.34$	$1.43 \pm 0.36$
$\tau^+ \rightarrow \mu^+\nu\bar{\nu}$	$1.1 \pm 0.1$	$1.60 \pm 0.24$	0
$D_s^+ \rightarrow \pi^+\pi^0\pi^0$	1.1 (estimate)	0.12	0.12
$D_s^+ \rightarrow K^0\pi^+$	$0.24 \pm 0.03$	$1.3 \pm 0.3$	$1.1 \pm 0.3$
$D_s^+ \rightarrow \eta\pi^+$	$1.5 \pm 0.2$	$1.1 \pm 0.3$	$0.9 \pm 0.3$
Sum		$6.2 \pm 0.7$	$3.5 \pm 0.6$

### III. LEPTONIC BRANCHING FRACTIONS

The result of the two-dimensional unbinned maximum likelihood fit to the sum of the  $MM^2$  distributions for case (i) and case (ii) is shown in Fig. 14. The other dimension in the fit is the invariant mass spectrum. Here we constrain the  $\tau^+\nu/\mu^+\nu$  ratio to the Standard Model value. From the fit we extract  $235.5 \pm 13.8$   $\mu^+\nu$  signal events. The efficiency is given by the product of the tracking and particle identification efficiencies, equal to 86.7%, the maximum extra photon energy cut of 300 MeV, equal to 98.7% and the tag bias of 105.2%, giving an

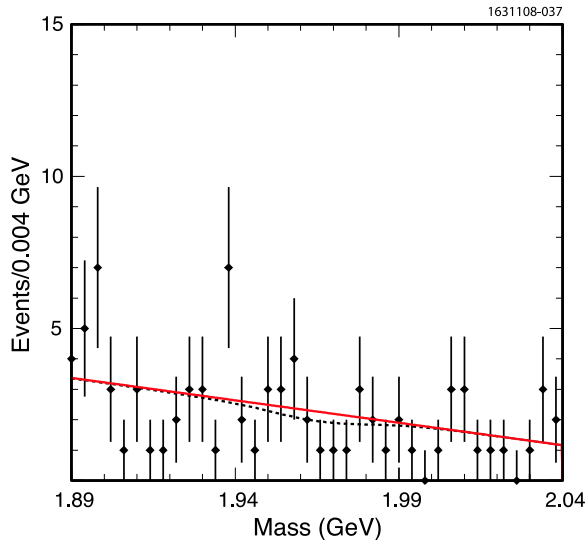


FIG. 12: The invariant  $\pi^+\pi^0$  mass. The curves show results of a fit using a linear background (solid) plus Gaussian signal function (dashed), where the width of the Gaussian is fixed to a value determined by Monte Carlo simulation.

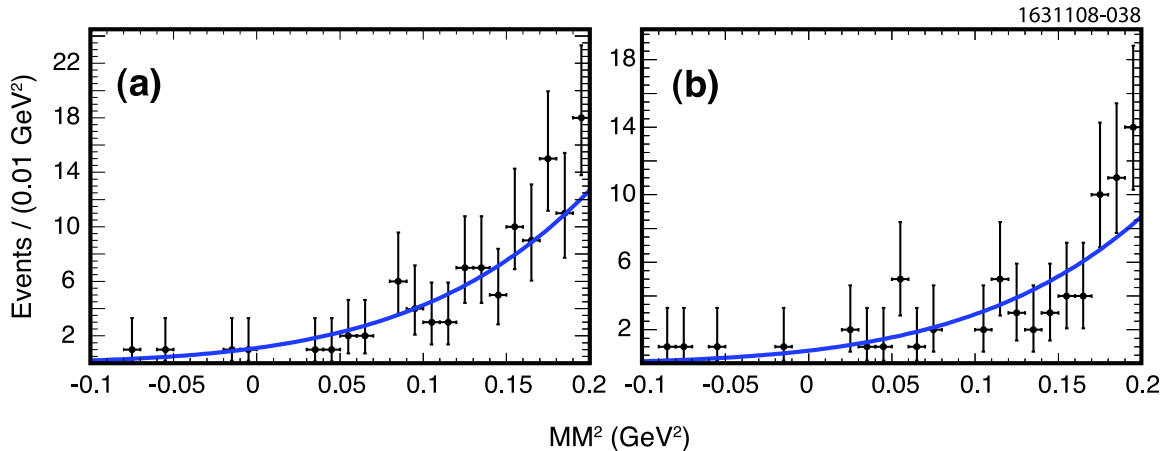


FIG. 13: The background rates for real  $D_s^+$  decays from Monte Carlo as a function of  $MM^2$  for case (i) and case (ii). The data are fit to quadratic polynomials.

overall efficiency of 90.0%. Using our tag sample of  $43859 \pm 936$  events, we find an effective branching ratio

$$\mathcal{B}^{\text{eff}}(D_s^+ \rightarrow \mu^+\nu) = (0.597 \pm 0.037 \pm 0.017)\% \quad (8)$$

The radiative correction of 1% reduces this to

$$\mathcal{B}^{\text{eff}}(D_s^+ \rightarrow \mu^+\nu) = (0.591 \pm 0.037 \pm 0.018)\% \quad (9)$$

(From now on we will only quote radiatively corrected results in this paper.) This is our most accurate result within the context of the Standard Model.

We can also analyze the data by not constraining the  $\tau^+\nu/\mu^+\nu$  ratio. We then fit the

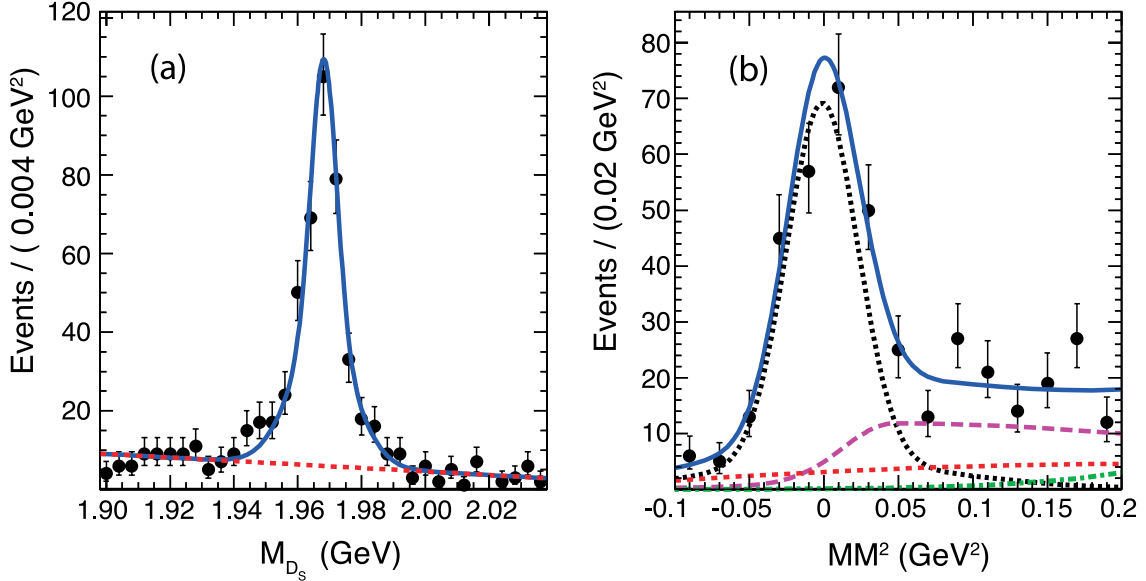


FIG. 14: The results of the two-dimensional fit to the sum of case (i) and case (ii) data. The data are shown as points with error bars. (a) The projection of the invariant mass distribution; the straight dashed line shows the background while the curve is the sum of the background and a two-Gaussian signal function. (b) The projection of the  $MM^2$  distribution; the dotted (black) curve is the two-Gaussian signal function for  $\mu^+\nu$ , the long-dashed (purple) curve shows the  $\tau^+\nu$ ,  $\tau^+ \rightarrow \pi^+\bar{\nu}$  signal, the dashed (red) line shows the background from non- $D_s^-$  events below the signal peak, while the dot-dashed (green) curve shows the background from real  $D_s^+$  events. The solid (blue) curve represents the sum of all contributions.

case (i) distribution and find

$$\mathcal{B}(D_s^+ \rightarrow \mu^+\nu) = (0.565 \pm 0.045 \pm 0.017)\% \quad (10)$$

The results of the fit are shown in Fig. 15.

By simultaneously fitting the case (i) and case (ii) distributions, constraining the ratio of  $\mu^+\nu$  events to be 98.8:1.2 and the ratio of  $\tau^+\nu$  events to be 55:45, in the two cases, respectively, we find  $125.6 \pm 15.7$   $\tau^+\nu$ ,  $\tau^+ \rightarrow \pi^+\bar{\nu}$  events. Using  $\mathcal{B}(\tau^+ \rightarrow \pi^+\bar{\nu}) = (10.90 \pm 0.07)\%$  [12], we measure

$$\mathcal{B}(D_s^+ \rightarrow \tau^+\nu) = (6.42 \pm 0.81 \pm 0.18)\% \quad (11)$$

The fit results are shown in Fig. 16.

The systematic errors on these branching fractions are given in Table III. The error on track finding is determined from a detailed comparison of the simulation with double tag events where one track is ignored. The particle identification on the  $\mu^+$  track arises from the fact that we veto kaons. The error on the photon veto efficiency, due to the 300 MeV/c extra shower energy cut, is determined using double tag events where both  $D_s^-$  and  $D_s^+$  are reconstructed in the same modes that we use for tagging. What we measure is a product of the efficiencies for two events each with different tags. This is translated into an efficiency for a single tags. The error on the number of tags  $\pm 2\%$  is assigned by varying the fitting functions and ranges. In addition there is a small error of  $\pm 0.6\%$  on the  $\tau^+\nu$  branching

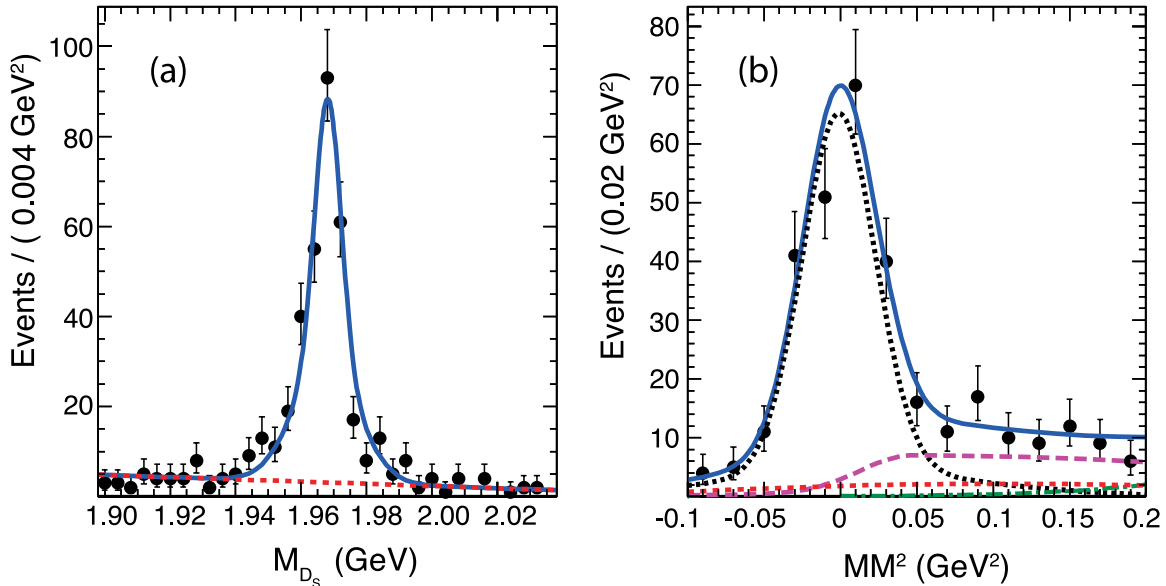


FIG. 15: The results of the two-dimensional fit to the case (i) data. The data are shown as points with error bars. (a) The projection of the invariant mass distribution; the straight dashed line shows the background while the curve is the sum of the background and a two-Gaussian signal function. (b) The projection of the  $MM^2$  distribution; the dotted (black) curve is the two-Gaussian signal function for  $\mu^+\nu$ , the long-dashed (purple) curve shows the  $\tau^+\nu$ ,  $\tau^+ \rightarrow \pi^+\bar{\nu}$  signal, the dashed (red) line shows the background from non- $D_s^-$  events below the signal peak, while the dot-dashed (green) curve shows the background from real  $D_s^+$  events. The solid (blue) curve represents the sum of all contributions.

fraction due to the uncertainty on the  $\tau^+$  decay fraction to  $\pi^+\bar{\nu}$ . Additional systematic errors arising from the background estimates are at the 1% level. The error on the radiative correction is taken as 100% of its value of 1%. When we use only one of the two cases to find a result an additional 1% error is included due to the minimum ionization discrimination of 300 MeV in the calorimeter.

TABLE III: Systematic errors on determination of the  $D_s^+ \rightarrow \mu^+\nu$  branching fraction.

Error Source	Size (%)
Track finding	0.7
Particle identification of $\mu^+$	1.0
$MM^2$ width	0.2
Photon veto	0.4
Background	1.0
Number of tags	2.0
Tag bias	1.0
Radiative Correction	1.0
Total	3.0

Lepton universality in the Standard Model requires that the ratio  $R$  from Eq. (2) be equal

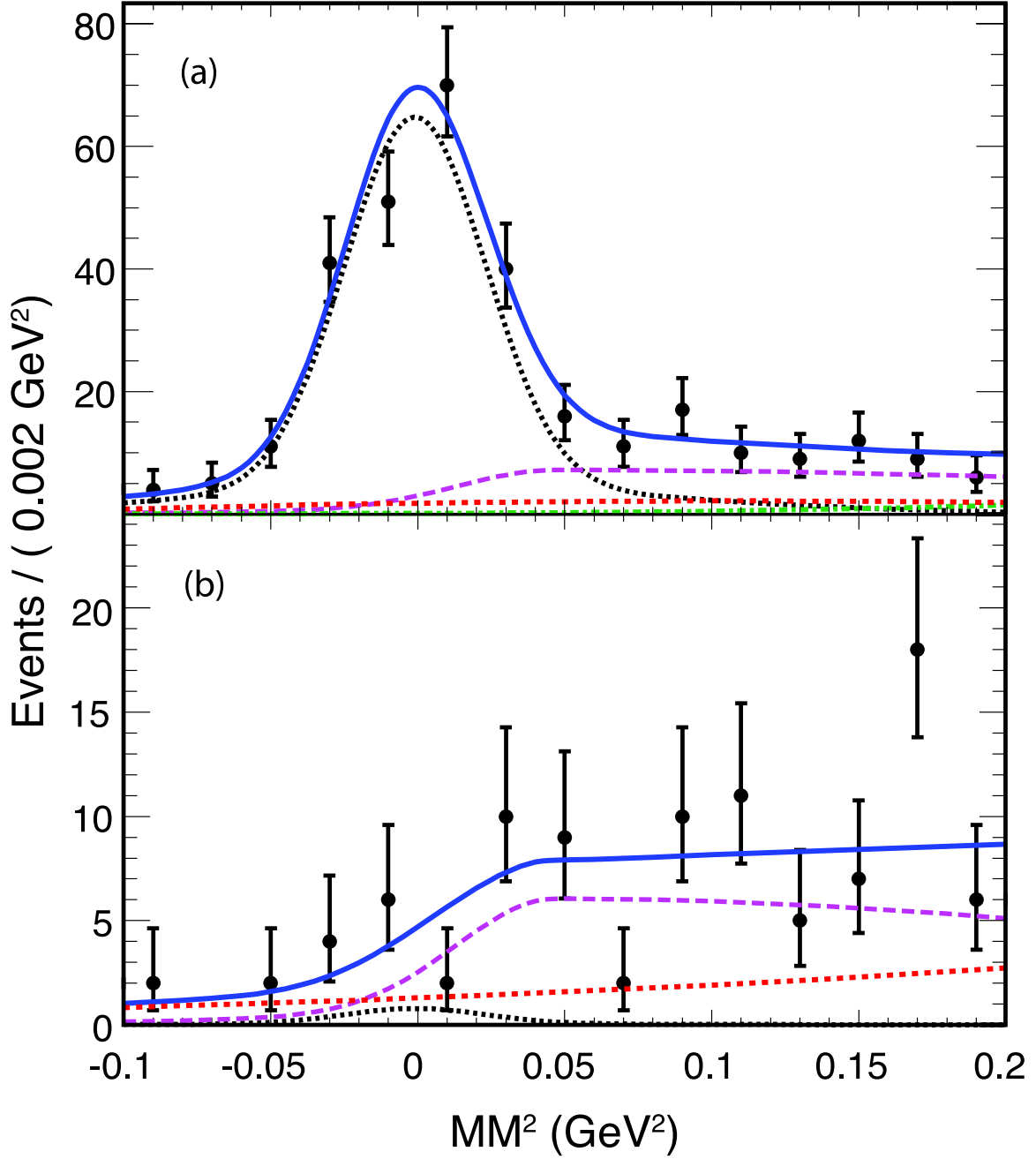


FIG. 16: The  $MM^2$  distributions from the two-dimensional fit done simultaneously to (a) case (i) and (b) case (ii) data. The data are shown as points with error bars. The dotted (black) curve is the two-Gaussian signal function for  $\mu^+\nu$ , the long-dashed (purple) curve shows the  $\tau^+\nu, \tau^+\pi^+\bar{\nu}$  signal, the dashed (red) line shows the background from non- $D_s^-$  events below the signal peak, while the dot-dashed (green) curve shows the background from real  $D_s^+$  events. The solid (blue) curve represents the sum of all contributions.

to a value of 9.76. We measure

$$R \equiv \frac{\Gamma(D_s^+ \rightarrow \tau^+\nu)}{\Gamma(D_s^+ \rightarrow \mu^+\nu)} = 11.4 \pm 1.7 \pm 0.2 . \quad (12)$$

Here the systematic error is dominated by the uncertainty on the minimum ionization cut that we use to separate the  $\mu^+\nu$  and  $\tau^+\nu$  regions at 300 MeV. We take this error as 2%, since a change here affects both the numerator and denominator. The ratio is consistent with the Standard Model prediction. Current results on  $D^+$  leptonic decays also show no deviations [9].

We also measure the CP violating asymmetry. The fit constraining the  $\tau^+\nu/\mu^+\nu$  ratio to the SM value of 9.76 yields  $124.5 \pm 9.9$   $\mu^+\nu$  and  $110.8 \pm 9.6$   $\mu^-\bar{\nu}$  events. We also find  $21807 \pm 581$   $D_s^-$  tags and  $21370 \pm 581$   $D_s^+$  tags. Then

$$\frac{\Gamma(D_s^+ \rightarrow \mu^+\nu) - \Gamma(D_s^- \rightarrow \mu^-\bar{\nu})}{\Gamma(D_s^+ \rightarrow \mu^+\nu) + \Gamma(D_s^- \rightarrow \mu^-\bar{\nu})} = 0.048 \pm 0.061 , \quad (13)$$

showing no evidence of CP violation.

The one detected electron opposite to our tags allows us to set an upper limit of

$$\mathcal{B}(D_s^+ \rightarrow e^+\nu) < 1.2 \times 10^{-4} \quad (14)$$

at 90% confidence level; this is also consistent with Standard Model predictions and lepton universality.

#### IV. CHECKS OF THE METHOD

We perform an overall check of our procedures by measuring  $\mathcal{B}(D_s^+ \rightarrow \bar{K}^0 K^+)$  which has been previously determined. For this measurement we compute the  $MM^2$  [Eq. (6)] using events with an additional charged track but here identified as a kaon. These track candidates have momenta of approximately 1 GeV/c; here our RICH detector has a pion to kaon fake rate of 1.1% with a kaon detection efficiency of 88.5% [25]. For this study, we do not veto events with neutral energy deposits  $>300$  MeV, or with less than three additional tracks beyond the tag, because of the presence of the  $K^0$ .

Events from the  $\eta\pi^+$  mode where the  $\pi^+$  fakes a  $K^+$  are very rare and would not peak at the proper  $MM^2$ . The mode  $\eta K^+$  does contribute a background at a somewhat higher  $MM^2$  of 0.30 GeV<sup>2</sup> and causes a small asymmetric tail on the high side of the peak. The branching fraction measured by CLEO is  $(0.14 \pm 0.03)\%$  [34]. We predict a total of  $47 \pm 10$  events from this source, that we include as a fixed component in our fit.

We perform the same two-dimension fit in invariant mass and  $MM^2$  as used for the  $\mu^+\nu$  signal, except that here the  $MM^2$  is calculated with respect to the  $K^+$  hypothesis, and an additional  $\eta K^+$  component is added. The  $MM^2$  distribution for events in the signal  $MM^{*2}$  region is shown in Fig. 9. The peak near 0.25 GeV<sup>2</sup> is due to the decay mode of interest. The backgrounds are the same as defined for the  $\mu^+\nu$  distributions above.

The fit yields  $1036 \pm 41$  events. In order to compute the branching fraction we use the efficiency of detecting the kaon track, 77.0%, including radiation [35], the particle identification efficiency of 88.5%, and take into account that it is easier to detect tags in events containing

a  $\bar{K}^0 K^+$  decay than in the average  $D_s D_s^*$  event due to the track and photon multiplicities, which gives a 3% correction.<sup>2</sup> These rates are estimated by using Monte Carlo simulation. We determine

$$\mathcal{B}(D_s^+ \rightarrow \bar{K}^0 K^+) = (3.06 \pm 0.14 \pm 0.09)\%, \quad (15)$$

where the systematic errors are listed in Table IV. We estimate the error from the signal shape by taking the change in the number of events when varying the signal width of the two-Gaussian function by  $\pm 1\sigma$ . The error on the background shapes is given by varying the shape of the background fit. The error on the particle identification efficiency is measured using two-body  $D^0$  decays [25]. The other errors are the same as described in Table III. Again, the largest component of the systematic error arises from the number of tag events (2%). In fact, to use this result as a check on our procedures, we need only consider the systematic errors that are different here than in the  $\mu^+\nu$  case. Those are due only to the signal and background shapes, the  $\eta K^+$  contribution and the particle identification cut. Those systematic errors are small.

To determine absolute branching fractions of charm mesons, CLEO-c uses a method where both particles are fully reconstructed (so called ‘‘double tags’’) and the rates are normalized using events where only one particle is fully reconstructed. Our result using this method for  $\mathcal{B}(D_s^+ \rightarrow K_S^0 K^+) = (1.49 \pm 0.07 \pm 0.05)\%$ , which when doubled becomes  $(2.98 \pm 0.14 \pm 0.10)\%$  [31]. This is in excellent agreement with the number in Eq. (15). These results are not independent.

TABLE IV: Systematic errors on determination of the  $D_s^+ \rightarrow \bar{K}^0 K^+$  branching fraction.

Error Source	Size (%)
Track finding	0.7
Particle identification of $\mu^+$	1.0
$\eta K^+$ branching fraction	0.6
MM <sup>2</sup> width	0.2
Background	1.0
Number of tags	2.0
Tag bias	1.0
Total	2.8

We also performed the entire analysis on a Monte Carlo sample that corresponds to an integrated luminosity 8 times larger than the data sample. The input branching fraction in the Monte Carlo is 0.61% for  $\mu^+\nu$  and 5.99% for  $\tau^+\nu$ , while our analysis measured  $\mathcal{B}^{\text{eff}}(D_s^+ \rightarrow \mu^+\nu) = (0.607 \pm 0.013)\%$  for  $\mu^+\nu$  and  $\tau^+\nu$  combined. The individual rates are  $\mathcal{B}(D_s^+ \rightarrow \mu^+\nu) = (0.615 \pm 0.016)\%$ , and  $\mathcal{B}(D_s^+ \rightarrow \tau^+\nu) = (6.02 \pm 0.27)\%$ .

<sup>2</sup> The tag bias is less here than in the  $\mu^+\nu$  case because of the  $K^0$  decays and interactions in the detector.

## V. THE DECAY CONSTANT AND CONCLUSIONS

Using our most precise value for  $\mathcal{B}(D_s^+ \rightarrow \mu^+\nu)$  from Eq. (8), that is derived using both our  $\mu^+\nu$  and  $\tau^+\nu$  samples, and Eq. (1) with a  $D_s$  lifetime of  $(500 \pm 7) \times 10^{-15}$  s [12], we extract

$$f_{D_s^+} = 263.3 \pm 8.2 \pm 3.9 \text{ MeV}. \quad (16)$$

This result has been radiatively corrected. These results supersede all our previous measurements of the  $D_s^+ \rightarrow \mu^+\nu$  and  $D_s^+ \rightarrow \tau^+\nu$ ,  $\tau^+ \rightarrow \pi^+\nu$  branching fractions which use data samples that are subsumed in this paper. Using the CLEO-c result based on an analysis of  $D_s^+ \rightarrow \tau^+\nu$ ,  $\tau^+ \rightarrow e^+\nu\bar{\nu}$  [2], of  $f_{D_s^+} = (252.5 \pm 11.1 \pm 5.2)$  MeV, we derive a CLEO-c average value of

$$f_{D_s^+} = 259.5 \pm 6.6 \pm 3.1 \text{ MeV}. \quad (17)$$

We combine with our  $D^+$  result [9]

$$f_{D^+} = 205.8 \pm 8.5 \pm 2.5 \text{ MeV} \quad (18)$$

and find a value for

$$\frac{f_{D_s^+}}{f_{D^+}} = 1.26 \pm 0.06 \pm 0.02, \quad (19)$$

where only a small part of the systematic error cancels in the ratio of our two measurements. Our new measurements are compared with other measurements in Table V.

TABLE V: Our results for  $\mathcal{B}(D_s^+ \rightarrow \mu^+\nu)$ ,  $\mathcal{B}(D_s^+ \rightarrow \tau^+\nu)$ , and  $f_{D_s^+}$  compared with previous measurements. Results have been updated for the new value of the  $D_s$  lifetime of 0.5 ps [12]. ALEPH combines both measurements to derive a value for the decay constant. (This table adopted from Table I of ref. [7].)

Exp.	Mode	$\mathcal{B}$	$\mathcal{B}_{\phi\pi}$ (%)	$f_{D_s^+}$ (MeV)
CLEO-c	$\mu^+\nu$	$(5.65 \pm 0.45 \pm 0.17) \cdot 10^{-3}$		$257.3 \pm 10.3 \pm 3.9$
CLEO-c	$\tau^+\nu$	$(6.42 \pm 0.81 \pm 0.18) \cdot 10^{-2}$		$278.7 \pm 17.1 \pm 3.8$
CLEO-c	combined above 2 results using SM			$263.3 \pm 8.2 \pm 3.9$
CLEO-c [2]	$\tau^+\nu$	$(5.30 \pm 0.47 \pm 0.22) \cdot 10^{-2}$		$252.5 \pm 11.1 \pm 5.2$
CLEO-c	combined all CLEO-c results			$259.5 \pm 6.6 \pm 3.1$
Belle <sup>†</sup> [21]	$\mu^+\nu$	$(6.38 \pm 0.76 \pm 0.52) \cdot 10^{-3}$		$274 \pm 16 \pm 12$
Average of CLEO and Belle results above, radiatively corrected				$261.2 \pm 6.9$
CLEO [14]	$\mu^+\nu$	$(6.2 \pm 0.8 \pm 1.3 \pm 1.6) \cdot 10^{-3}$	$3.6 \pm 0.9$	$273 \pm 19 \pm 27 \pm 33$
BEATRICE [15]	$\mu^+\nu$	$(8.3 \pm 2.3 \pm 0.6 \pm 2.1) \cdot 10^{-3}$	$3.6 \pm 0.9$	$312 \pm 43 \pm 12 \pm 39$
ALEPH [16]	$\mu^+\nu$	$(6.8 \pm 1.1 \pm 1.8) \cdot 10^{-3}$	$3.6 \pm 0.9$	$282 \pm 19 \pm 40$
ALEPH [16]	$\tau^+\nu$	$(5.8 \pm 0.8 \pm 1.8) \cdot 10^{-2}$		
L3 [17]	$\tau^+\nu$	$(7.4 \pm 2.8 \pm 1.6 \pm 1.8) \cdot 10^{-2}$		$299 \pm 57 \pm 32 \pm 37$
OPAL [18]	$\tau^+\nu$	$(7.0 \pm 2.1 \pm 2.0) \cdot 10^{-2}$		$283 \pm 44 \pm 41$
BaBar [19]	$\mu^+\nu$	$(6.74 \pm 0.83 \pm 0.26 \pm 0.66) \cdot 10^{-3}$	$4.71 \pm 0.46$	$283 \pm 17 \pm 7 \pm 14$

<sup>†</sup> This result has been radiatively corrected by multiplying the measured branching ratio by 99%.

Most measurements of  $D_s^+ \rightarrow \ell^+ \nu$  are normalized with respect to  $\mathcal{B}(D_s^+ \rightarrow \phi \pi^+) \equiv \mathcal{B}_{\phi\pi}$ . An exception is the OPAL measurement which is normalized to the  $D_s$  fraction in  $Z^0$  events that is derived from an overall fit to heavy flavor data at LEP [33]. It still, however, relies on absolute branching fractions that are hidden by this procedure, and the estimated error on the normalization is somewhat smaller than that indicated by the error on  $\mathcal{B}_{\phi\pi}$  available at the time of their publication. The L3 measurement is normalized taking the fraction of  $D_s$  mesons produced in  $c$  quark fragmentation as  $0.11 \pm 0.02$ , and the ratio of  $D_s^*/D_s$  production of  $0.65 \pm 0.10$ . The ALEPH results use  $\mathcal{B}_{\phi\pi}$  for their  $\mu^+ \nu$  results and a similar procedure as OPAL for their  $\tau^+ \nu$  results. We note that the recent BaBar result uses a larger  $\mathcal{B}_{\phi\pi}$  than the other results. The CLEO-c determination of  $f_{D_s^+}$  using the modes in this paper is the most accurate to date.

Theoretical models that predict  $f_{D_s^+}$  and the ratio  $\frac{f_{D_s^+}}{f_{D^+}}$  are listed in Table VI. Upper limits

TABLE VI: Theoretical predictions of  $f_{D_s^+}$ ,  $f_{D^+}$ , and  $f_{D_s^+}/f_{D^+}$ . QL indicates quenched lattice calculations. (This table adopted from Table II of ref. [7].)

Model	$f_{D_s^+}$ (MeV)	$f_{D^+}$ (MeV)	$f_{D_s^+}/f_{D^+}$
Lattice (HPQCD+UKQCD) [6]	$241 \pm 3$	$208 \pm 4$	$1.162 \pm 0.009$
Lattice (FNAL+MILC+HPQCD) [5]	$249 \pm 3 \pm 16$	$201 \pm 3 \pm 17$	$1.24 \pm 0.01 \pm 0.07$
QL (QCDSF) [37]	$220 \pm 6 \pm 5 \pm 11$	$206 \pm 6 \pm 3 \pm 22$	$1.07 \pm 0.02 \pm 0.02$
QL (Taiwan) [38]	$266 \pm 10 \pm 18$	$235 \pm 8 \pm 14$	$1.13 \pm 0.03 \pm 0.05$
QL (UKQCD) [39]	$236 \pm 8_{-14}^{+17}$	$210 \pm 10_{-16}^{+17}$	$1.13 \pm 0.02_{-0.02}^{+0.04}$
QL [40]	$231 \pm 12_{-1}^{+6}$	$211 \pm 14_{-12}^{+2}$	$1.10 \pm 0.02$
QCD Sum Rules [41]	$205 \pm 22$	$177 \pm 21$	$1.16 \pm 0.01 \pm 0.03$
QCD Sum Rules [42]	$235 \pm 24$	$203 \pm 20$	$1.15 \pm 0.04$
Field Correlators [43]	$210 \pm 10$	$260 \pm 10$	$1.24 \pm 0.03$
Quark Model [44]	268	234	1.15
Quark Model [45]	$248 \pm 27$	$230 \pm 25$	$1.08 \pm 0.01$
LFQM (Linear) [46]	211	248	1.18
LFQM (HO) [46]	194	233	1.20
LF-QCD [47]	253	241	1.05
Potential Model [48]	241	238	1.01
Isospin Splittings [49]		$262 \pm 29$	

on  $f_{D^+}$  and  $f_{D_s}$  of 230 and 270 MeV, respectively, have been determined using two-point correlation functions by Khodjamirian [36]. Our result for  $f_{D_s}$  is higher than most theoretical expectations. The average of this new  $f_{D_s^+}$  result with the CLEO-c result based on the decay mode  $D_s^+ \rightarrow \tau^+ \nu$ ,  $\tau^+ \rightarrow e^+ \nu \bar{\nu}$ , is  $(259.5 \pm 7.3)$  MeV (see Table V). This rate differs by 2.3 standard deviations from the Follana *et al.* prediction [6], and is close to, but does not saturate the Khodjamirian bound. (Averaging in the Belle result for  $D_s^+ \rightarrow \mu^+ \nu$ , which is also an absolute branching fraction measurement raises the difference to 2.6 standard deviations.) If the difference with Follana *et al.* were to persist with the advent of more precise measurements it could be explained by a deficiency in the Lattice calculation, or physics beyond the Standard Model. (We note that both unquenched LQCD calculations agree with CLEO's result for  $f_{D^+}$ .) Either of the two leptoquark models of Dobrescu and

Kronfeld could explain a discrepancy in the  $D_s^+$  case [8]. They also have a charged Higgs model. Hewett [13], and Akeroyd and Chen [11] pointed out that leptonic decay widths are modified by new physics. Specifically, for the  $D^+$  and  $D_s^+$ , in the case of the two-Higgs doublet model (2HDM), Eq. (1) is modified by a factor  $r_q$  multiplying the right-hand side:

$$r_q = \left[ 1 + \left( \frac{1}{m_c + m_q} \right) \left( \frac{M_{D_q}}{M_{H^+}} \right)^2 (m_c - m_q \tan^2 \beta) \right]^2, \quad (20)$$

where  $m_{H^+}$  is the charged Higgs mass,  $M_{D_q}$  is the mass of the  $D$  meson (containing the light quark  $q$ ),  $m_c$  is the charm quark mass,  $m_q$  is the light-quark mass, and  $\tan \beta$  is the ratio of the vacuum expectation values of the two Higgs doublets. (Here we modified the original formula of [11] to take into account the charm quark coupling [50].) To get an enhancement in the rate, the  $m_c$  term must be inducing the effect, which implies that both the  $D^+$  and  $D_s^+$  would see a similar effect in contradiction to the trends in our data. Another explanation in a model based on R-parity violating supersymmetry has been given by Kundu and Nandi [51].

## VI. ACKNOWLEDGMENTS

We gratefully acknowledge the effort of the CESR staff in providing us with excellent luminosity and running conditions. D. Cronin-Hennessy and A. Ryd thank the A.P. Sloan Foundation. This work was supported by the National Science Foundation, the U.S. Department of Energy, the Natural Sciences and Engineering Research Council of Canada, and the U.K. Science and Technology Facilities Council. We thank C. Davies, B. Dobrescu, A. Kronfeld, P. Lepage, P. Mackenzie, R. Van de Water, and R. Zwicky for useful discussions.

- 
- [1] M. Artuso *et al.*, (CLEO), Phys. Rev. Lett. **99**, 071802 (2007); T. Pedlar *et al.*, (CLEO), Phys. Rev. D **76**, 072002 (2007).
- [2] P. U. E. Onyisi *et al.*, (CLEO), “Improved Measurement of Absolute Branching Fraction of  $D_s^+ \rightarrow \tau^+ \nu_\tau$ ,” CLNS 08/2043, arXiv:0901.1147 [hep-ex].
- [3] D. Silverman and H. Yao, Phys. Rev. D **38**, 214 (1988).
- [4] I. S. Towner and J. C. Hardy, Phys. Rev. C **77**, 025501 (2008).
- [5] C. Aubin *et al.*, Phys. Rev. Lett. **95**, 122002 (2005).
- [6] E. Follana, C. T. H. Davies, G. P. Lepage, and J. Shigemitsu (HPQCD and UKQCD), Phys. Rev. Lett. **100**, 062002 (2008), arXiv:0706.1726 [hep-lat].
- [7] J. L. Rosner and S. Stone, “Decay Constants of Charged Pseudoscalar Mesons,” in PDG 2008, C. Amsler *et al.*, Physics Letters **B667**, 1 (2008), see also arXiv:0802.1043 [hep-ex].
- [8] B. A. Dobrescu and A. S. Kronfeld, Phys. Rev. Lett. **100**, 241802 (2008), arXiv:0803.0512 [hep-ph].
- [9] B. I. Eisenstein *et al.* (CLEO), Phys. Rev. D **78**, 052003 (2008) [arXiv:0806.2112v2] [hep-ex] (2008).
- [10] G. Buchalla, A. J. Buras and M. E. Lautenbacher, Rev. Mod. Phys. **68**, 1125 (1996) [hep-ph/9512380].
- [11] A. G. Akeroyd, Prog. Theor. Phys. **111**, 295 (2004)[hep-ph/0308260]; A. G. Akeroyd and C. H. Chen, Phys. Rev. D **75**, 075004 (2007), [hep-ph/0701078].
- [12] C. Amsler *et al.*, Physics Letters **B667**, 1 (2008).
- [13] J. L. Hewett, “Searching For New Physics with Charm,” SLAC-PUB-95-6821 (1995) [hep-ph/9505246]; W.-S. Hou, Phys. Rev. D **48**, 2342 (1993).
- [14] M. Chadha *et al.* (CLEO), Phys. Rev. D **58**, 032002 (1998).
- [15] Y. Alexandrov *et al.* (BEATRICE), Phys. Lett. B **478**, 31 (2000).
- [16] A. Heister *et al.* (ALEPH) Phys. Lett. B **528**, 1 (2002) [hep-ex/0201024].
- [17] M. Acciarri *et al.* (L3), Phys. Lett. B **396**, 327 (1997).
- [18] G. Abbiendi *et al.* (OPAL), Phys. Lett. B **516**, 236 (2001).
- [19] B. Aubert *et al.* (BABAR), Phys. Rev. Lett. **98**, 141801 (2007), [hep-ex/0607094].
- [20] S. Stone, “Hadronic Charm Decays and  $D$  Mixing,” invited talk at Flavor Physics and CP Violation Conference, Vancouver, 2006, eConf C060409 [hep-ph/0605134].
- [21] K. Abe *et al.*, (Belle), Phys. Rev. Lett. **100**, 221801 (2008), [arXiv:0709.1340].
- [22] G. Burdman, T. Goldman and D. Wyler, Phys. Rev. D **51**, 111 (1995) [hep-ph/9405425].
- [23] E. Barberio and Z. Was, Comput. Phys. Commun. **79**, 291 (1994), version 2.15 with interference enabled.
- [24] D. Peterson *et al.*, Nucl. Instrum. and Meth. **A478**, 142 (2002); Y. Kubota *et al.* (CLEO Collaboration), Nucl. Instrum. and Meth. **A320**, 66 (1992).
- [25] M. Artuso *et al.*, Nucl. Instrum. Meth. **A554**, 147 (2005) [physics/0506132].
- [26] D. Cronin-Hennessy *et al.* (CLEO), “Measurement of Charm Production Cross Sections in  $e^+e^-$  Annihilation at Energies between 3.97 and 4.26 GeV,” arXiv:0801.3418 [hep-ex].
- [27] M. Artuso *et al.* (CLEO), Phys. Rev. Lett. **95**, 251801 (2005) [hep-ex/0508057].
- [28] T. Skwarnicki, “A Study of the Radiative Cascade Transitions Between the Upsilon-Prime and Upsilon Resonances,” DESY F31-86-02 (thesis, unpublished) (1986).

- [29] P. Rubin *et al.* (CLEO), Phys. Rev. D **73**, 112005 (2006) [hep-ex/0604043].
- [30] G. Bonvicini *et al.* (CLEO) Phys. Rev. D **70**, 112004 (2004) [hep-ex/0411050].
- [31] J.P. Alexander *et al.* (CLEO), Phys. Rev. Lett., **100**, 161804 (2008) arXiv:0801.0680 [hep-ex].
- [32] S. Malvezzi (FOCUS), “Dalitz Plot Analysis in the FOCUS Experiment,” J. Phys. Conf. Ser. **9**, 165 (2005).
- [33] ALEPH, DELPHI, L3, and OPAL Collaborations, Nucl. Instr. and Meth. **A378**, 101 (1996).
- [34] G. S. Adams *et al.* (CLEO), Phys. Rev. Lett. **99**, 191805 (2007) arXiv:0708.0139 [hep-ex].
- [35] E. Barberio, B. van Eijk, Z. Was, Comput. Phys. Commun. **66**, 115 (1991); E. Barberio and Z. Was, Comput. Phys. Commun. **79**, 291 (1994).
- [36] A. Khodjamirian [arXiv:0812.3747v1] [hep-ph].
- [37] A. Ali Khan *et al.* (QCDSF), Phys. Lett. **B652**, 150 (2007) [hep-lat/0701015].
- [38] T. W. Chiu *et al.*, Phys. Lett. **B624**, 31 (2005) [hep-ph/0506266].
- [39] L. Lellouch, C.-J. Lin and C. J. David (UKQCD), Phys. Rev. D **64**, 094501 (2001).
- [40] D. Becirevic *et al.*, Phys. Rev. D **60**, 074501 (1999).
- [41] J. Bordes, J. Peñarrocha, and K. Schilcher, Journal of High Energy Physics, **511**, 14 (2005) [hep-ph/0507241].
- [42] S. Narison, “Light and Heavy Quark Masses, Flavour Breaking of Chiral Condensates, Meson Weak Leptonic Decay Constants in QCD,” [hep-ph/0202200] (2002).
- [43] A. M. Badalian *et al.*, Phys. Rev. D **75**, 116001 (2007) [hep-ph/0702157]; see also A. M. Badalian and B. L. G. Bakker, “The Ratios  $f_{D_s}/f_D$  and  $f_{B_s}/f_B$  As a Test of The Running Mass  $m_s$  At Low Scale,” [hep-ph/0702229].
- [44] D. Ebert *et al.*, Phys. Lett. B **635**, 93 (2006).
- [45] G. Cvetič *et al.*, Phys. Lett. B **596**, 84 (2004).
- [46] H.-M. Choi, Phys. Rev. D **75**, 073016 (2007) [hep-ph/0701263], uses “Light Front Quark Model,” with either linear or harmonic oscillator (HO) potential .
- [47] L. Salcedo *et al.*, Braz. J. Phys. **34**, 297 (2004).
- [48] Z. G. Wang *et al.*, Nucl. Phys. **A744**, 156 (2004).
- [49] J. Amundson *et al.*, Phys. Rev. D **47**, 3059 (1993).
- [50] A. Kronfeld, private communication.
- [51] A. Kundu and S. Nandi, Phys. Rev. D **78**, 015009 (2008) [arXiv:0803.1898v1] [hep-ph].